

# SCIENTIFIC REPORTS

OPEN

## Evaluation of CdZnTeSe as a high-quality gamma-ray spectroscopic material with better compositional homogeneity and reduced defects

Utpal N. Roy<sup>1</sup>, Giuseppe S. Camarda<sup>1</sup>, Yonggang Cui<sup>1</sup>, Rubi Gul<sup>1</sup>, Ge Yang<sup>1,3</sup>, Jakub Zazvorka<sup>ID 2</sup>, Vaclav Dedic<sup>2</sup>, Jan Franc<sup>2</sup> & Ralph B. James<sup>1,4</sup>

X- and gamma-ray detectors have broad applications ranging from medical imaging to security, non-proliferation, high-energy physics and astrophysics. Detectors with high energy resolution, e.g. less than 1.5% resolution at 662 keV at room temperature, are critically important in most uses. The efficacy of adding selenium to the cadmium zinc telluride (CdZnTe) matrix for radiation detector applications has been studied. In this paper, the growth of a new quaternary compound  $\text{Cd}_{0.9}\text{Zn}_{0.1}\text{Te}_{0.98}\text{Se}_{0.02}$  by the Traveling Heater Method (THM) is reported. The crystals possess a very high compositional homogeneity with less extended defects, such as secondary phases and sub-grain boundary networks. Virtual Frisch-grid detectors fabricated from as-grown ingots revealed ~0.87–1.5% energy resolution for 662-keV gamma rays. The superior material quality with a very low density of defects and very high compositional homogeneity heightens the likelihood that  $\text{Cd}_{0.9}\text{Zn}_{0.1}\text{Te}_{0.98}\text{Se}_{0.02}$  will be the next generation room-temperature detector material.

Radiation detectors are critically needed in applications of medical imaging, security, non-proliferation, astrophysics and high-energy physics<sup>1–7</sup>. All these applications demand high-performance detectors at a reasonably low cost. Most radiation detector materials are categorized into two classes, scintillators and semiconductors. Semiconductor-based detectors outperform scintillators in terms of efficiency per unit volume, energy resolution and proportionality of gamma-ray energies and pulse height.

The requirements for semiconductor materials in X- and gamma-ray detector applications are very stringent. An ideal material should be composed of elements with high atomic number to ensure sufficient absorption of gamma rays; its band-gap should be high to fulfill the requirement of high resistivity of the material at room temperature to achieve low dark current without cooling; and, the material should have excellent charge-transport characteristics to ensure full charge collection. As opposed to semiconductor sensors for low-energy photons, radiation detectors need to be thick enough to ensure sufficient absorption of high-energy X and gamma rays within the active volume of the detector. Thus, detector materials should have the lowest possible defects (charge trapping centers), so that the induced charge carriers can travel through the entire length of the detector without being trapped. In addition, to produce detectors at low cost, materials ought to be produced with high production yield, requiring high compositional uniformity in the as-grown materials. To meet these challenges, researchers have been exploring suitable radiation detector materials for more than four decades. So far, only a handful of materials evolved as prospective candidates<sup>8–13</sup> such as  $\text{HgI}_2$ , CdTe, CdZnTe and TlBr. Very recently,  $\text{CsPbBr}_3$  (3.8% at 662 keV) was reported to be a promising material<sup>14</sup> for this purpose, but its energy resolution still needs to be improved. Among these materials, cadmium zinc telluride ( $\text{Cd}_{0.9}\text{Zn}_{0.1}\text{Te}$ , CZT) is still the most successful material that is being used commercially. In the last three decades, intense efforts have been invested to improve the material properties of CZT. However, CZT technology still suffers from three major detrimental defects including compositional inhomogeneity due to the non-unity segregation coefficient (~1.35)<sup>15</sup> of Zn, the presence of a high concentration of secondary phases, and high concentrations of sub-grain boundaries/

<sup>1</sup>Brookhaven National Laboratory, Upton, NY, 11973, USA. <sup>2</sup>Institute of Physics, Charles University, Ke Karlovu 5, Prague, 121 16, Czech Republic. <sup>3</sup>Present address: North Carolina State University, Raleigh, NC, 27695-7909, USA.

<sup>4</sup>Present address: Savannah River National Laboratory, Aiken, SC, 29808, USA. Correspondence and requests for materials should be addressed to U.N.R. (email: [uroy@bnl.gov](mailto:uroy@bnl.gov))

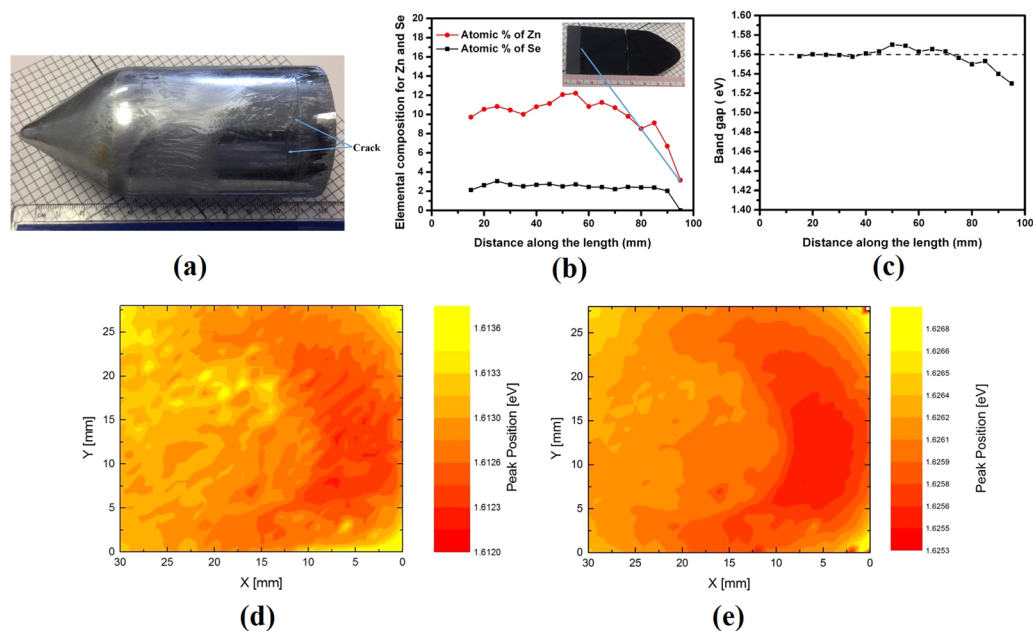


**Figure 1.** (a) As-grown  $\text{Cd}_{0.9}\text{Zn}_{0.1}\text{Te}_{0.98}\text{Se}_{0.02}$  ingot with 52-mm diameter, grown by the THM, (b) Variation of Zn and Se (atomic %) along the length of the ingot, (c) Calculated band-gap along the length of the ingot. The inset shows the wafer cut along the length of the as-grown  $\text{Cd}_{0.9}\text{Zn}_{0.1}\text{Te}_{0.98}\text{Se}_{0.02}$  ingot, and the map of PL peak energy positions at 7 K for the as-grown  $\text{Cd}_{0.9}\text{Zn}_{0.1}\text{Te}_{0.98}\text{Se}_{0.02}$  wafer cut perpendicular to the growth axis, (d) ( $A^\circ$ , X) peak mapping and (e) ( $D^\circ$ , X) peak mapping. The mapping area is  $\sim 2.8 \times 3.0 \text{ cm}^2$ .

dislocation walls in the CZT matrix. Thus, the production yield of CZT suffers from the compositional inhomogeneity, while the secondary phases and the sub-grain boundary networks severely affect the charge collection and hence degrade the spectral response<sup>16,17</sup>. These defects result in the high cost of CZT materials and limit the widespread deployment of the technology.

As compared to other melt-growth methods, mainly the Bridgman growth technique, the traveling heater method (THM) is the most common means to grow CZT crystals commercially. The main detriment of THM-grown CZT ingots is that wafers need post-growth annealing to achieve detector-grade quality<sup>18</sup>. This additional process further increases the production cost of the material. Recently we observed that the addition of selenium in the CdTe matrix greatly reduces the sub-grain boundary network and secondary-phase concentration, and thus improves the compositional uniformity<sup>19–21</sup>.

To solve the issues presently limiting the deployment of CZT technology, the advantages of adding Se to the CZT matrix were explored. Here we report the growth of  $\text{Cd}_{0.9}\text{Zn}_{0.1}\text{Te}_{0.98}\text{Se}_{0.02}$  (CZTS) by the traveling heater method. The addition of Se was found to have profound effects in reducing the sub-grain boundary network and the secondary-phase concentration. Furthermore, the achieved compositional homogeneity in both axial and radial directions was observed over about 90% of the ingot volume. Virtual Frisch-grid CZTS detectors were fabricated from as-grown CZTS crystals; outstanding energy resolutions of  $\sim 0.87\%$  at 662 keV were achieved without reliance on pulse-processing algorithms to correct for electron trapping. Hence, we can successfully eliminate the need for a post-growth annealing process as used extensively for THM-grown CZT, while also achieving excellent transport properties.

## Results

The  $\text{Cd}_{0.9}\text{Zn}_{0.1}\text{Te}_{0.98}\text{Se}_{0.02}$  crystals were grown by the THM technique. The ingots are  $\sim 52 \text{ mm}$  in diameter, weighing about 1.0–1.2 Kg (Fig. 1a). In general, the ingots are crack-free except near the Te-CZTS interface, as indicated by the arrows in Fig. 1a. The occurrence of these cracks is most likely due to the different thermal expansion coefficients of Te and CZTS leading to thermoelastic stress.

The composition vis. the band-gap of the CZTS ingot was found to be uniform for  $\sim 90\%$  of the total length of the ingot (Fig. 1b,c), as measured by Energy Dispersive X-ray Analysis (EDAX). The wafer cut along the length of the ingot is shown in the inset of Fig. 1b. In view of the experimental accuracy of EDAX at  $\sim \pm 1$  atomic %<sup>22</sup>, a high degree of uniformity in the composition was achieved for  $\sim 90\%$  of the ingot length. Considerable depletion of Zn within  $\sim 1 \text{ cm}$  near the Te-rich CZTS interface was observed (Fig. 1b). The band-gap of the material was estimated along the length of the ingot from the measured composition by EDAX, using the empirical formula by Brill *et al.*<sup>23</sup>, for the  $\text{Cd}_{1-x}\text{Zn}_x\text{Te}_{1-y}\text{Se}_y$  quaternary compound at room temperature.

$$E_{g(x,y)} = 1.511 - 0.54y + 0.6x \quad (x, y \leq 0.10) \quad (1)$$

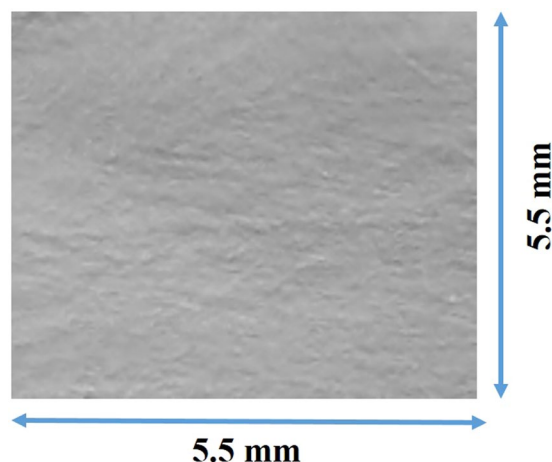


**Figure 2.** X-ray topographic image of an as-grown  $\text{Cd}_{0.9}\text{Zn}_{0.1}\text{Te}_{0.98}\text{Se}_{0.02}$  sample. Exposed area:  $\sim 5.5 \times 5.5 \text{ mm}^2$ .

where, 1.511 eV was considered to be the band gap of CdTe at room temperature. According to the Eq. 1, the theoretical band gap of  $\text{Cd}_{0.9}\text{Zn}_{0.1}\text{Te}_{0.98}\text{Se}_{0.02}$  quaternary compound is about 0.011 eV lower as compared to  $\text{Cd}_{0.9}\text{Zn}_{0.1}\text{Te}$ .

Within the 1-cm region near the interface of the ingot, inevitable cracks occur for all THM grown CdTe-based ingots concomitant to the large thermal expansion coefficient difference between Te-rich CZT/CZTS alloy and CZT/CZTS. The high compositional uniformity along the length of the ingot ensures a higher yield as compared to CZT, where the zinc composition has a considerable wider variability. The compositional uniformity of THM-grown CZT with similar growth parameters was reported to be slightly more than one third of the total length of the ingot<sup>24</sup>. The incorporation of selenium is effective in modifying the segregation coefficient of Zn in CZTS ingot, so that it is closer to unity compared to CZT. To further investigate the radial compositional uniformity, we performed mapping of the low-temperature photoluminescence (PL) across the as-grown  $\text{Cd}_{0.9}\text{Zn}_{0.1}\text{Te}_{0.98}\text{Se}_{0.02}$  wafer cut perpendicular to the ingot axis, cut about 2 cm below the interface. The spatial variation of the composition highly reflects the band-gap of the material. The PL peak energy positions are very sensitive to the band-gap, hence the composition of the material. The PL mapping was performed at Charles University, Prague. The typical PL spectrum (taken at 7 K) consists of a dominant acceptor-bound exciton ( $A^\circ$ , X), a donor-bound exciton ( $D^\circ$ , X) peak and the peak corresponding to the A-center (Supplementary Fig. 1). An area of about  $2.8 \times 3.0 \text{ cm}^2$  was scanned for the two-inch-diameter as-grown  $\text{Cd}_{0.9}\text{Zn}_{0.1}\text{Te}_{0.98}\text{Se}_{0.02}$  wafer cut perpendicular to the ingot axis. The spatial variation of the peak energy positions, viz. the map of peak energy at different positions of the scanned area with the step size of 1 mm, for the ( $A^\circ$ , X) and ( $D^\circ$ , X) peaks over the  $2.8 \times 3.0 \text{ cm}^2$  area are plotted in Fig. 1d,e respectively. For both the ( $A^\circ$ , X) and ( $D^\circ$ , X) peaks, the spatial peak energy variations ( $\Delta E$ ) are within 0.0015 eV over the scanned area of  $\sim 2.8 \times 3.0 \text{ cm}^2$ . The observed small spatial variation of less than 0.0015 eV for both the ( $A^\circ$ , X) and ( $D^\circ$ , X) peaks confirms the excellent compositional uniformity for the as-grown quaternary compound  $\text{Cd}_{0.9}\text{Zn}_{0.1}\text{Te}_{0.98}\text{Se}_{0.02}$ .

An X-ray topographic technique was used to investigate the crystalline defects, such as sub-grain boundaries and their networks using the beamline 3.3.2 at Lawrence Berkeley National Laboratory's (LBNL) Advanced Light Source (ALS). Figure 2 shows a representative X-ray topographic image of exposed area  $\sim 5.5 \times 5.5 \text{ mm}^2$  taken from the single crystalline sample of dimensions  $\sim 5.6 \times 5.6 \times 12 \text{ mm}^3$ , cut from a single grain from the as-grown  $\text{Cd}_{0.9}\text{Zn}_{0.1}\text{Te}_{0.98}\text{Se}_{0.02}$  ingot. Any presence of sub-grain boundary and their network, are generally visible in X-ray topographic image by white and/or black lines. The white lines correspond to the separation of the diffracted images of the adjacent sub-grains, while the dark lines correspond to the overlap of the diffracted images depending on the crystallographic tilt of the adjacent sub-grains. As illustrated, the sample is completely free from sub-grain boundary networks. For CZT, on the other hand are generally found to be highly decorated with sub-grain boundaries and their network<sup>17</sup>. For CdTeSe ingots grown by THM also we observed very few sub-grain boundaries and absence of sub-grain boundary network as revealed by X-ray topography<sup>21</sup>.

The occasional presence of an individual sub-grain boundary was observed in some regions of CZTS samples, but no sub-grain boundary network was detected. The absence of sub-grain boundary network and occasional presence of sub-grain boundaries in Se containing compounds such as CdTeSe and in the present case in  $\text{Cd}_{0.9}\text{Zn}_{0.1}\text{Te}_{0.98}\text{Se}_{0.02}$ , are very encouraging and elucidates that Se plays an important role in effective solid solution hardening of the matrix. Tanaka *et al.*<sup>25</sup>, reported decrease of lattice constant and also observed the effective solution hardening upon introduction of Se in CdZnTe matrix. The dislocation density was observed to be much lower and the absence of any cellular structure for Se containing compound<sup>25</sup>. The cellular structures are in general generate at the dislocation walls and are very common in CdTe and/or CdZnTe compounds.

The charge-transport characteristics such as mobility-lifetime product of electrons  $(\mu\tau)_e$  in the as-grown CZTS material was evaluated at room temperature for an Au/CZTS/Au planar detector. The  $(\mu\tau)_e$  value was extracted by fitting the Hecht equation to the charge collection plot for an  $^{241}\text{Am}$  gamma source at an energy of 59.6 keV. The typical spectrum from an  $^{241}\text{Am}$  gamma source is shown in Supplementary Fig. 2, under the applied

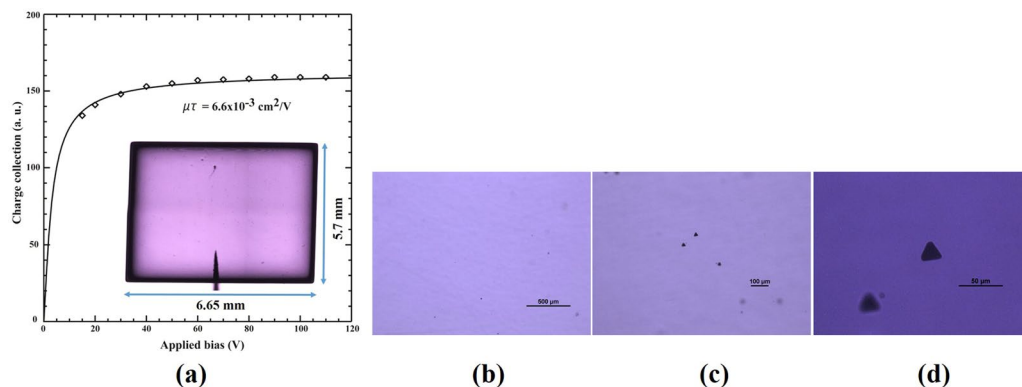


**Figure 3.** (a) Plot of the charge collection versus applied bias for the as-grown CZTS planar detector at room temperature. The 59.6-keV line was used from an  $^{241}\text{Am}$  source. The solid line indicates the Hecht fitting to extract the  $\mu\tau$  value for electrons, the inset in Fig. 1a shows the IR transmission image of the whole sample of dimensions  $\sim 6.65 \times 5.7 \times 1.86 \text{ mm}^3$ , (b–d) high magnification IR transmission microscopic images of an as-grown CZTS sample showing triangular Te inclusions.

bias of  $-50 \text{ V}$ . The  $(\mu\tau)_e$  obtained for the as-grown CZTS planar detector,  $\sim 6.65 \times 5.7 \times 1.86 \text{ mm}^3$ , was  $6.6 \times 10^{-3} \text{ cm}^2/\text{V}$  (Fig. 3a). The presence of Te inclusions was investigated by Infra-Red (IR) transmission microscopy. The IR transmission image of the entire sample is shown in the inset of Fig. 3a. As evident from the IR transmission image, very few Te inclusions are present in the as-grown CZTS. For comparison, very high concentrations of Te inclusions are generally reported to be present in the as-grown CZT grown by the same technique<sup>26</sup>. The high magnification IR transmission microscopic pictures are shown in Fig. 3b,c, depicting the presence of very few Te inclusions. The shape of the Te inclusions are triangular (Fig. 3c,d), which is typical for CZT-based material. The size of the inclusions was found to be about  $16\text{--}20 \mu\text{m}$  with very low concentrations. The high magnification IR transmission microscopic images for different regions of the CZTS sample (Supplementary Fig. 3) reveal the absence of any large inclusions. A significant reduction of Te inclusions was confirmed through IR transmission microscopy as compared to as-grown CZT.

The detector quality of the as-grown  $\text{Cd}_{0.9}\text{Zn}_{0.1}\text{Te}_{0.98}\text{Se}_{0.02}$  material was appraised by fabricating detectors with a virtual Frisch grid geometry. The dark current-voltage relationship (I–V) at room temperature for an emblematic Frisch-grid CZTS detector with dimensions of  $\sim 4.5 \times 4.5 \times 10.8 \text{ mm}^3$  shows very low leakage current ( $\sim 0.63 \text{ nA}$ ) under an applied bias of  $500 \text{ V}$  (Fig. 4a). The resistivity measured from the slope of the I–V plot for a  $\pm 1 \text{ V}$  (Supplementary Fig. 4) range was  $\sim 2.9 \times 10^{10} \text{ ohm-cm}$ , which fulfills the requirement for high resistivity detector-grade material. The fabricated detector with the Frisch-grid length of  $3 \text{ mm}$  was evaluated with various gamma sources with energies ranging from  $31 \text{ keV}$  to  $1.33 \text{ MeV}$ . The  $662\text{-keV}$  gamma energy line from  $^{137}\text{Cs}$  source is generally considered as the standard in evaluating gamma detectors. The energy resolution at  $662 \text{ keV}$  of a detector with various shaping times was evaluated, and the best energy resolution was achieved with a shaping time of  $2 \mu\text{s}$  (Fig. 4b). Very high-resolution spectroscopic performance with energy resolution of  $\sim 1.07\%$  at  $662 \text{ keV}$  was achieved (Fig. 4c) under an applied bias of  $3000 \text{ V}$  across the detector length ( $10.8 \text{ mm}$ ) with a shaping time of  $2 \mu\text{s}$ . The energy resolutions for the same detector at  $662 \text{ keV}$  with shaping times of  $1$  and  $3 \mu\text{s}$  obtained were within  $1.2\%$ . The peak-to-valley and peak-to-Compton ratios were  $28$  and  $5.6$  respectively (Fig. 4c), demonstrating excellent detector quality. The stability of the detector performance was examined by operating the detector at  $3000 \text{ V}$  and acquiring pulse height spectra at various time intervals ranging from  $10$  to  $1000 \text{ sec}$ . A very stable energy resolution ( $\sim 1.1\%$ ), peak-to-valley and peak-to-Compton ratios for the measured  $662\text{-keV}$  gamma line were achieved for the entire period of operation (Supplementary Fig. 5a,b). The sharp feature of the electronic pulse (Fig. 4c) indicates very low noise for the detector even under an applied bias of  $3000 \text{ V}$ . The  $511\text{-keV}$  and  $1.275\text{-MeV}$  gamma rays from a  $^{22}\text{Na}$  source were measured by the detector showing an excellent energy resolution of  $1.34\%$  and  $\sim 1\%$  respectively (Fig. 4d,e). All the gamma lines from a  $^{133}\text{Ba}$  source including the  $31\text{-keV}$  X-ray line were successfully identified by the as-grown CZTS detector with very high energy resolution (Fig. 4f,g). The energy resolution at  $31 \text{ keV}$  was  $\sim 9\%$ , while for the  $81\text{-keV}$  and  $356\text{-keV}$  peaks, the corresponding values are  $4.6\%$  and  $1.6\%$  respectively. The CZTS detector resolved high energy gamma lines at energies of  $1.17 \text{ MeV}$  and  $1.33 \text{ MeV}$  from a  $^{60}\text{Co}$  source with energy resolutions of  $\sim 1.1\%$  and  $1.0\%$  respectively (Fig. 4h). The detector quality of the as-grown CZTS material is comparable to very high quality commercially available CZT detectors. All the pulse height spectra from different sources presented here are as-measured, i.e., without any charge-loss corrections.

## Conclusions

The efficacy of adding Se to the CZT matrix for radiation detector applications has been successfully demonstrated. Selenium was effective in modifying the segregation coefficient of Zn, resulting in higher compositional homogeneity along the length of ingots as opposed to  $\text{CdZnTe}$ . The higher compositional homogeneity offers remarkable potential to increase the overall production yield of CZTS material at a lower cost. Selenium was seen to be very effective in reducing the secondary phases (Te inclusions) in the grown CZTS ingots and in lattice hardening resulting in CZTS ingots free from sub-grain boundary networks. The secondary phases and the

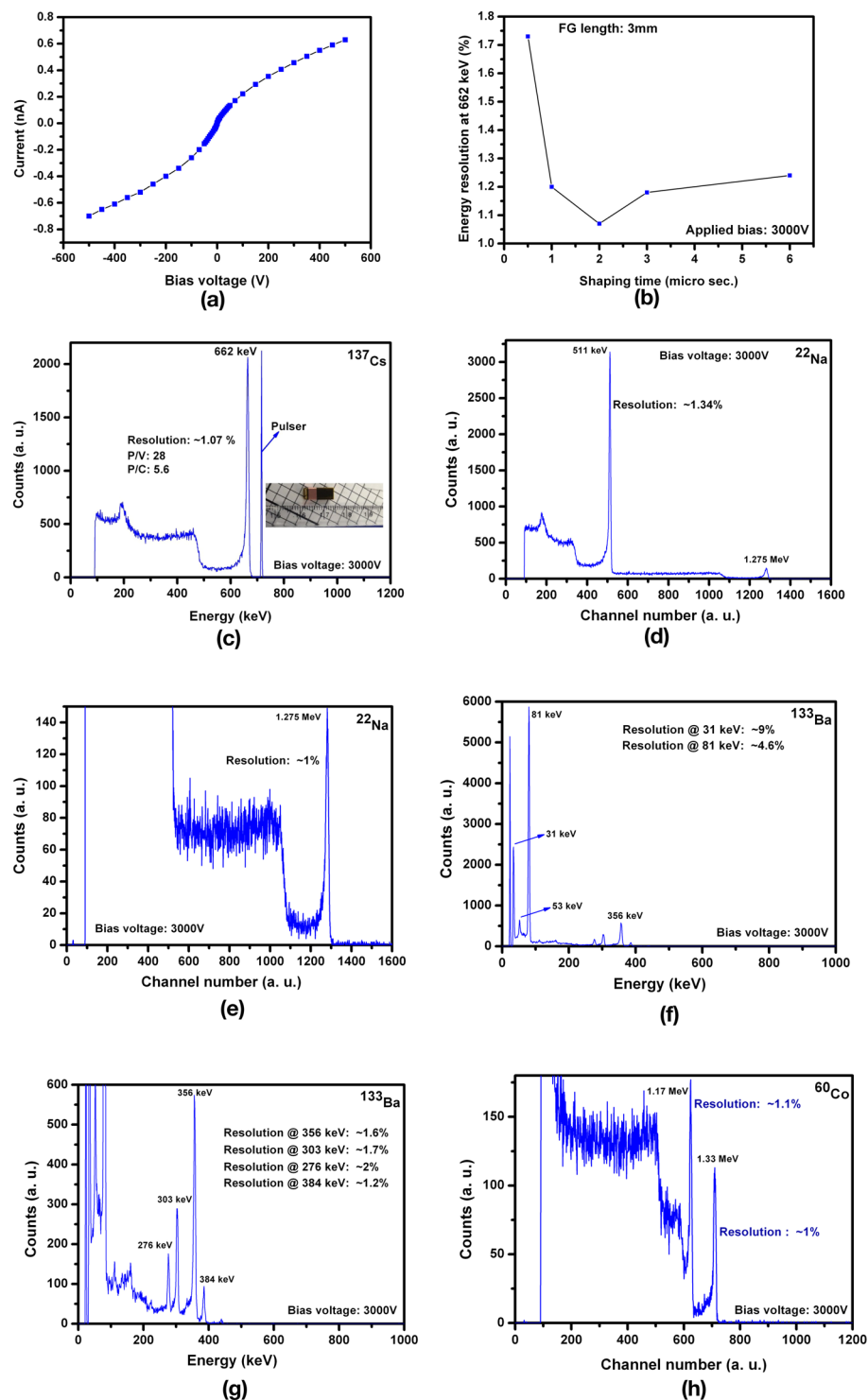


**Figure 4.** Current-voltage characteristics and gamma response for the Frisch grid detector fabricated from an as-grown CZTS ingot at room temperature. **(a)** Dark I–V characteristics of the detector sample at room temperature, **(b)** Detector response (energy resolution at 662 keV) at different shaping times, **(c)** Pulse height spectrum for the Frisch grid detector from a  $^{137}\text{Cs}$  source, the inset shows the photograph of the detector, **(d)** Pulse height spectrum for the Frisch grid detector for a  $^{22}\text{Na}$  source, **(e)** Zoomed version of the same spectrum to enhance the high energy peak, **(f)** Pulse height spectrum for the Frisch grid detector for a  $^{133}\text{Ba}$  source, **(g)** Zoomed version of the same spectrum to enhance the high energy peaks, and **(h)** Pulse height spectrum for the Frisch grid detector for a  $^{60}\text{Co}$  source showing very well resolved high energy gamma lines at energies of  $\sim 1.17$  MeV and  $1.33$  MeV. The detector dimensions are:  $\sim 4.5 \times 4.5 \times 10.8$  mm<sup>3</sup>.



sub-grain boundary networks are the major issues affecting the performance and cost of CZT detector technology. Both types of defects are deleterious and are known to hinder the charge transport characteristics, resulting in severe degradation of the detector performance. The addition of Se was found to be very effective in resolving the decade-long issues suffered by CZT. The reduced density of Te inclusions and the absence of sub-grain boundary networks in CZTS material makes it a promising approach to increase the yield of high-quality detectors. Well-resolved high-resolution gamma lines in the energy range of 31 keV to 1.33 MeV were observed for virtual Frisch grid as-grown CZTS detectors, demonstrating the excellent material properties, including high compositional homogeneity, a very low concentration of Te inclusions and the absence of sub-grain boundary networks.

## Methods

The  $\text{Cd}_{0.9}\text{Zn}_{0.1}\text{Te}_{0.98}\text{Se}_{0.02}$  compound was first synthesized from a stoichiometric amount of 6N purity  $\text{Cd}_{0.9}\text{Zn}_{0.1}\text{Te}$  from 5N Plus Inc. and 6N purity CdSe from Azelis Inc. The THM growth was carried out from 6N purity Te-rich solution with In as the dopant. Both 6N purity Te and In were procured from Alfa Aesar. Prior to synthesis and growth by THM, the inner walls of the ampoules were coated with carbon by cracking spectroscopic grade acetone at  $\sim 900^\circ\text{C}$ , followed by annealing the coated ampoules at  $\sim 1150^\circ\text{C}$  for one hour. The ampoules were then loaded with the required amount of materials and sealed under dynamic vacuum of  $\sim 2 \times 10^{-6}$  torr. All the CZTS crystals were grown with 52-mm inner diameter using conically tipped, high purity quartz ampoules. The THM growth runs were carried out in a three-zone furnace with growth parameters similar to those used for CZT growth<sup>27</sup>. The ingots were grown with a lowering rate of 3–3.5 mm/day, and the temperature gradient near the interface was maintained between 10–15°C/cm. After completion of the growth, the ingots were cooled down to room temperature at a rate of  $\sim 100^\circ\text{C}/\text{day}$ .

The grown ingots were cut into pieces using a diamond-impregnated wire saw to different sizes for various characterizations. The cut samples were then polished with successive grit size SiC paper and finally polished with 0.05- $\mu\text{m}$  alumina suspension on felt pad to achieve mirror-finish surfaces. IR transmission microscopic studies were carried out using a Nikon, Eclipse LV 100 Microscope. Compositional analyses were performed using a Jeol 7600 electron microscope equipped with Energy Dispersive Spectroscopy. White Beam X-ray Diffraction Topography (WBXDT) measurements were carried out at LBNL's ALS Beamline 3.3.2 with an X-ray beam energy ranging from 4 keV to 25 keV. The X-ray topographic measurements were carried out in reflection mode. The schematic of the experimental setup has been illustrated in our previous publication<sup>21</sup>. The samples used for the topographic experiments were cut from single crystalline grains. The low-temperature PL mapping was carried out at Charles University using a Radius (Coherent) diode laser for excitation of the sample, with the excitation energy of 1.95 eV having power of 25 mW. The beam area used for excitation was  $\sim 0.25\text{ mm}^2$ . The sample was raster scanned with the step size of 1 mm. For both topographic and PL mapping experiments, the samples were etched in 2% bromine methanol solution for two minutes to remove any possible damaged layer that might be introduced during the polishing process. A Keithley 6487 picoammeter/voltage source was used for the dark current-voltage measurements.

## Data Availability

The data supporting this study are available from the authors on reasonable request.

## References

- Schlesinger, T. E. *et al.* Cadmium zinc telluride and its use as a nuclear radiation detector material. *Materials Science and Engineering R* **32**, 103 (2001).
- Yang, G. & James, R. B. *Physics, Defects, Hetero- and Nano-structures, Crystal Growth, Surfaces and Applications Part II*, (EDAX. Triboulet R. *et al.*) 214 (Elsevier, 2009).
- Wilson, M. D. *et al.* A 10 cm  $\times$  10 cm CdTe Spectroscopic Imaging Detector based on the HEXITEC ASIC. *J. Instrumentation* **10**, 10011 (2015).
- Iniewski, K. CZT sensors for Computed Tomography: from crystal growth to image quality. *J. Instrumentation* **11**, C12034 (2016).
- Burger, A. *et al.* Development of portable CdZnTe spectrometers for remote sensing of signatures from nuclear materials. *Phys. Status Solidi C* **2**, 1586 (2005).
- Holstensson, H. *et al.* Model-based correction for scatter and tailing effects in simultaneous  $^{99\text{m}}\text{Tc}$  and  $^{123}\text{I}$  imaging for a CdZnTe cardiac SPECT camera. *Phys. Med. Biol.* **60**, 3045 (2015).
- Krawczynski, H. S. *et al.* X ray polarimetry with the Polarization Spectroscopic Telescope Array (PolSTAR). *Astroparticle Phys.* **75**, 8 (2016).
- Piechotka, M. Mercuric iodide for room temperature radiation detectors. Synthesis, purification, crystal growth and defect formation. *Mat. Sc. & Engr.* **R18**, 1 (1997).
- Kargar, A. *et al.* Charge collection efficiency characterization of a  $\text{HgI}_2$  Frisch collar spectrometer with collimated high energy gamma rays. *Nucl. Instrum. Methods A* **652**, 186 (2011).
- Shiraki, H. *et al.* THM Growth and Characterization of 100 mm Diameter CdTe Single Crystals. *IEEE Trans. on Nucl. Sc.* **56**, 1717 (2009).
- Baudin, D. *et al.* D2R1: A 2-D X-Ray Detector for CdTe-Based Fine Pitch and High-Energy Resolution Imaging Spectroscopy. *IEEE Trans. on Nucl. Sc.* **65**, 1408 (2018).
- Chen, H. *et al.* Characterization of Traveling Heater Method (THM) Grown  $\text{Cd}_{0.9}\text{Zn}_{0.1}\text{Te}$  Crystals. *IEEE Trans. on Nucl. Sc.* **54**, 811 (2007).
- Hitomi, K. *et al.* TlBr Gamma-Ray Spectrometers Using the Depth Sensitive Single Polarity Charge Sensing Technique. *IEEE Trans. on Nucl. Sc.* **55**, 1781 (2008).
- He, Y. *et al.* High spectral resolution of gamma-rays at room temperature by perovskite  $\text{CsPbBr}_3$  single crystals. *Nature. Communications* **9**, 1609 (2018).
- Zhang, N. *et al.* Anomalous segregation during electrodynamic gradient freeze growth of cadmium zinc telluride. *J. Cryst. Growth* **325**, 10 (2011).
- Carini, G. A. *et al.* Effect of Te precipitates on the performance of CdZnTe detectors. *Appl. Phys. Lett.* **88**, 143515 (2006).
- Bolotnikov, A. E. *et al.* Characterization and evaluation of extended defects in CZT crystals for gamma-ray detectors. *J. Cryst. Growth* **379**, 46 (2013).

18. Chen, H. *et al.* Characterization of large cadmium zinc telluride crystals grown by traveling heater method. *J. Appl. Phys.* **103**, 014903 (2008).
19. Roy, U. N. *et al.* High compositional homogeneity of  $\text{CdTe}_{1-x}\text{Se}_x$  crystals grown by the Bridgman method. *APL Materials* **3**, 026102 (2015).
20. Roy, U. N. *et al.* Growth of  $\text{CdTe}_{1-x}\text{Se}_x$  from a Te-rich solution for applications in radiation detection. *J. Cryst. Growth* **386**, 43 (2014).
21. Roy, U. N. *et al.* Evaluation of  $\text{CdTe}_{1-x}\text{Se}_x$  crystals grown from a Te-rich solution. *J. Cryst. Growth* **389**, 99 (2014).
22. Peng, C. *et al.* Liquid-phase-epitaxy-grown  $\text{InAs}_x\text{Sb}_{1-x}/\text{GaAs}$  for room-temperature 8–12  $\mu\text{m}$  infrared detectors. *Appl. Phys. Lett.* **88**, 242108 (2006).
23. Brill, G. *et al.* Molecular Beam Epitaxial Growth and Characterization of Cd-Based II–VI Wide-Bandgap Compounds on Si Substrates. *J. Electronic Mat.* **34**, 655 (2005).
24. Roy, U. N. *et al.* Zinc mapping in THM grown detector grade CZT. *J. Cryst. Growth* **347**, 53 (2012).
25. Tanaka, A. *et al.* Zinc and selenium co-doped CdTe substrates lattice matched to HgCdTe. *J. Cryst. Growth* **94**, 166 (1989).
26. Roy, U. N. *et al.* Size and distribution of Te inclusions in THM as-grown CZT wafers: The effect of the rate of crystal cooling. *J. Cryst. Growth* **332**, 34 (2011).
27. Roy, U. N. *et al.* Growth of spectroscopic grade  $\text{Cd}_{0.9}\text{Zn}_{0.1}\text{Te}$ :In by THM technique. *J. Cryst. Growth* **312**, 33–36 (2009).

## Acknowledgements

This work was supported primarily by the U.S. Department of Energy, Office of Defense Nuclear Nonproliferation Research and Development, DNN R & D. JZ, VD, and JF acknowledge the support of the Grant Agency of Czech Republic under project. No. 18-06818S. The manuscript has been authored by Brookhaven Science Associates, LLC under Contract No. DE-SC0012704 with the U.S. Department of Energy.

## Author Contributions

U.N.R. conceived the idea and wrote the main manuscript text. G.S.C. and Y.C. performed the X-ray topographic measurements and analysis. U.N.R., R.G. and G.Y. were involved with sample preparation, and Te-inclusion studies. U.N.R., G.S.C. and Y.C. were involved in detector measurement and evaluation. J.Z., V.D. and J.F. were involved in measuring P.L. mapping and analysis. R.B.J., U.N.R. and J.F. were involved in the data analysis. All the authors participated in scientific discussions and critically reviewed the manuscript.

## Additional Information

**Supplementary information** accompanies this paper at <https://doi.org/10.1038/s41598-019-43778-3>.

**Competing Interests:** The authors declare no competing interests.

**Publisher's note:** Springer Nature remains neutral with regard to jurisdictional claims in published maps and institutional affiliations.



**Open Access** This article is licensed under a Creative Commons Attribution 4.0 International License, which permits use, sharing, adaptation, distribution and reproduction in any medium or format, as long as you give appropriate credit to the original author(s) and the source, provide a link to the Creative Commons license, and indicate if changes were made. The images or other third party material in this article are included in the article's Creative Commons license, unless indicated otherwise in a credit line to the material. If material is not included in the article's Creative Commons license and your intended use is not permitted by statutory regulation or exceeds the permitted use, you will need to obtain permission directly from the copyright holder. To view a copy of this license, visit <http://creativecommons.org/licenses/by/4.0/>.

© The Author(s) 2019